Non-modal stability analysis of low-Re separated flow around a NACA 4415 airfoil in ground effect

Wei He[a,c,*], José Miguel Pérez[b], Peng Yu[c], Larry K.B. Li[a]

[a] *The Hong Kong University of Science and Technology, Clear Water Bay, Hong Kong*
[b] *Universidad Politécnica de Madrid, Madrid, Spain*
[c] *Southern University of Science and Technology, Shenzhen, China*

Abstract

In this numerical–theoretical study, we perform a linear non-modal stability analysis of the separated flow around a NACA 4415 airfoil over a no-slip ground at low Reynolds numbers ($300 \leqslant Re \leqslant 500$) and high angles of attack ($12^\circ \leqslant \alpha \leqslant 20^\circ$). We find that: (i) the strength of the recirculation zone behind the airfoil is a key parameter controlling the absolute/convective nature of the instability in the boundary layer downstream; (ii) when Re, α or the ground clearance increases, the energy gain also increases, with the optimal perturbations switching from being three dimensional to two dimensional; and (iii) classical hairpin vortices, or Klebanoff modes, can be produced by three-dimensional optimal perturbations on a two-dimensional steady base flow containing a laminar separation bubble. Knowledge of the spatiotemporal features of the optimal mode could aid the design of advanced strategies for flow control. This study offers new insight into the transient growth behavior of airfoil–ground flow systems at low Re and high α, contributing to a better understanding of the ground-effect aerodynamics of small insects and micro aerial vehicles.

Keywords: transient growth, non-modal stability, ground effect, low Reynolds number

1. Introduction

Predicting laminar–turbulent transition in airfoil flows is a recognized challenge, particularly when massive flow separation occurs. Flow separation is known to reduce the aerodynamic performance of an airfoil, decreasing its lift and increasing its drag, as well as making the precise location of transition more difficult to predict. Nevertheless, predicting transition is important as it can facilitate the design of flow control strategies by enabling the optimal parameters of the system to be more readily determined [1, 2]. For some flows, modal stability analysis can accurately predict the long-time asymptotic behavior by determining the spatiotemporal response to small perturbations. However, for other flows (e.g.

*Corresponding author
Email address: mewhe@ust.hk (Wei He)

wall-bounded shear flows such as channel flow), modal stability analysis is known to fail because non-modal instabilities can dominate at short times [3, 4]. Such failure of asymptotic theory occurs because, in the latter type of flow, there is significant transient growth, which cannot be accounted for using a modal stability framework based on eigenvalues. Instead, non-modal stability analysis must be used, as has been recommended in Refs. [5, 6].

In linear non-modal stability analysis, small perturbations can lead to large transient growth of energy [7]. Luchini [8] examined a flat-plate boundary layer and determined its so-called optimal perturbations, i.e. the initial conditions that maximize energy growth in time. Cherubini et al. [9] investigated the relationship between non-normality and nonlinearity in a laminar separation bubble and showed, among other findings, that the non-normality of the modes is the physical reason that the bubble acts as an amplifier of small disturbances. Marquet et al. [10] and Blackburn et al. [11] investigated the transient growth associated with large separation bubbles in the flow over a backward-facing step. Non-modal analysis has also been used to explore the role of small initial perturbations on the stability of flows at low Reynolds numbers, including flow around a circular cylinder [12], flow around low-pressure turbine blades [13, 14, 15], and flow around NACA airfoils [16, 17, 18].

Linear BiGlobal stability analysis has shown that the laminar separated flow around a NACA 4415 airfoil at low Reynolds numbers ($200 \leqslant Re \leqslant 1000$) and high angles of attack ($18^\circ \leqslant \alpha \leqslant 20^\circ$) can be stabilized by the presence of a no-slip ground, with the eigenvalues being particularly sensitive to the ground clearance and Re [19, 20]. Furthermore, non-modal stability analysis of an analogous airfoil flow, but without a ground, has shown that the wake exhibits strong energy growth in response to two-dimensional (2D) or three-dimensional (3D) perturbations [18]. The optimal initial perturbations were found to be similar to those for flow around a cascade of low-pressure turbine blades [13, 18]. These linear optimal initial perturbations were found to evolve into the classical Kelvin–Helmholtz (KH) mode over a long time horizon [18]. However, the effect of a nearby ground on the non-modal stability characteristics of laminar separated flow around an airfoil has yet to be explored. Of particular interest is the energy produced by transient growth over a short time horizon, because if this is significant, it can potentially trigger early transition to turbulence [5, 3]. Therefore, it is important to determine the spatiotemporal characteristics of the optimal perturbations. This is the primary focus of the present study.

In Sec. 2, we present the theoretical framework underpinning linear non-modal stability analysis, as well as the numerical setup and boundary conditions used in this study. In Sec. 3, we present the base flow around a NACA 4415 airfoil at two Reynolds numbers, two ground clearances, and four angles of attack. We then discuss the results obtained from non-modal stability analysis. In Sec. 4, we conclude with the key findings and implications of this study.

2. Problem definition

2.1. Theoretical framework

The flow under study is governed by the non-dimensional incompressible Navier–Stokes and continuity equations:

$$\begin{aligned} \frac{\partial \mathbf{u}}{\partial t} + \mathbf{u}\cdot\nabla\mathbf{u} &= -\nabla p + \frac{1}{Re}\nabla^2\mathbf{u}, \\ \nabla\cdot\mathbf{u} &= 0, \end{aligned} \tag{1}$$

where the Reynolds number is defined as $Re \equiv U_\infty c/\nu$. Here U_∞ is the free-stream velocity, c is the chord length of the airfoil, and ν is the kinematic viscosity of the fluid. The dimensionless velocity vector $\mathbf{u}$ and pressure p are expressed as $\mathbf{q}(x,y,z,t) = (\mathbf{u},p)^{\mathrm{T}} = (u,v,w,p)^{\mathrm{T}}$, where x, y and z are the streamwise, cross-stream and spanwise directions, respectively.

Equation (1) is solved using direct numerical simulation (DNS), resulting in a steady or time-periodic 2D base flow $\bar{\mathbf{q}}(x,y,t) = (\bar{\mathbf{u}},\bar{p})^{\mathrm{T}}$, on which a linear BiGlobal stability analysis is performed [19, 21, 22]. This analysis uses infinitesimal unsteady 3D perturbations of the form $\tilde{\mathbf{q}}(x,y,z,t) = (\tilde{\mathbf{u}},\tilde{p})^{\mathrm{T}}$. The total field $\mathbf{q} = \bar{\mathbf{q}} + \epsilon\tilde{\mathbf{q}}$, where $\epsilon \ll 1$, is reconstructed by superimposing $\tilde{\mathbf{q}}$ onto $\bar{\mathbf{q}}$. Substituting this decomposition into Eq. (1) gives the linearized Navier–Stokes equations (LNSE):

$$\begin{aligned} \frac{\partial \tilde{\mathbf{u}}}{\partial t} + \bar{\mathbf{u}}\cdot\nabla\tilde{\mathbf{u}} + \tilde{\mathbf{u}}\cdot\nabla\bar{\mathbf{u}} &= -\nabla\tilde{p} + \frac{1}{Re}\nabla^2\tilde{\mathbf{u}}, \\ \nabla\cdot\tilde{\mathbf{u}} &= 0. \end{aligned} \tag{2}$$

In incompressible flow, the pressure disturbance is a function of the velocity disturbance, which implies that Eq. (2) can be expressed as:

$$\frac{\partial \tilde{\mathbf{u}}}{\partial t} = \mathcal{L}\tilde{\mathbf{u}}, \tag{3}$$

where $\mathcal{L}$ is a linear operator. For BiGlobal stability analysis, the 3D perturbation is defined to be spanwise periodic, $\tilde{\mathbf{u}}(x,y,z,t) = \hat{\mathbf{u}}(x,y)e^{i(\beta z-\omega t)} + c.c.$, where $\hat{\mathbf{u}}$ is the amplitude function, $\beta \equiv 2\pi/L_z$ is the wavenumber along the spanwise periodic length L_z, ω is the complex eigenvalue of the resulting generalized eigenvalue problem, and *c.c.* is the complex conjugate to ensure that the perturbation is real valued.

In non-modal stability analysis, the evolution of an initial perturbation $\tilde{\mathbf{u}}_0$ is governed by Eq. (3) such that:

$$\tilde{\mathbf{u}}(t) = \mathcal{A}(t)\tilde{\mathbf{u}}_0, \tag{4}$$

where $\mathcal{A}(t) = \exp(\mathcal{L}t)$ is an evolution operator enabling the evolution of the initial perturbation $\tilde{\mathbf{u}}_0$ to be determined at time instant t. The energy growth of $\tilde{\mathbf{u}}$ over time τ, which is

non-dimensionalized by the characteristic time c/U_∞, is defined as:

$$\begin{aligned} E(\tilde{\mathbf{u}}(\tau)) &= \frac{<\tilde{\mathbf{u}}, \tilde{\mathbf{u}}>}{2} \\ &= \frac{<\mathcal{A}(\tau)\tilde{\mathbf{u}}_0, \mathcal{A}(\tau)\tilde{\mathbf{u}}_0>}{2} \\ &= \frac{<\mathcal{A}^+(\tau)\mathcal{A}(\tau)\tilde{\mathbf{u}}_0, \tilde{\mathbf{u}}_0>}{2}, \end{aligned} \tag{5}$$

where $<,>$ is the L_2 inner product integrated over the flow domain, $\mathcal{A}^+$ is the adjoint operator of $\mathcal{A}$, and $\mathcal{A}^+\mathcal{A}$ is a normal matrix. Typically, the aim of non-modal stability analysis is to find the initial perturbation that maximizes the energy gain, i.e. the energy growth over a given finite time horizon τ:

$$G(\tau) = \max_{\tilde{\mathbf{u}}_0} \frac{<\mathcal{A}^+(\tau)\mathcal{A}(\tau)\tilde{\mathbf{u}}_0, \tilde{\mathbf{u}}_0>}{<\tilde{\mathbf{u}}_0, \tilde{\mathbf{u}}_0>}. \tag{6}$$

The perturbation $\tilde{\mathbf{u}}_0$ is the optimal perturbation at time 0 and is the eigenfunction of:

$$\mathcal{A}^+(\tau)\mathcal{A}(\tau)\tilde{\mathbf{u}}_0 = \sigma^2\tilde{\mathbf{u}}_0, \tag{7}$$

whose dominant eigenvalue is σ^2. This optimal perturbation is also the singular eigenvalue of $\mathcal{A}(\tau)$ [7]. The term $\tilde{\mathbf{u}}_\tau = \mathcal{A}(\tau)\tilde{\mathbf{u}}_0$ is the corresponding final optimal perturbation after evolving over time interval τ [23].

Given a 3D perturbation, a Fourier expansion is performed in the spanwise direction, $\tilde{u}(x, y, z, t) = \tilde{u}(x, y, t)\exp(i\beta z)$, where β is the spanwise wavenumber, as mentioned earlier.

2.2. Flow geometry, computational domain, and boundary conditions

The flow geometry and computational domain used in the present non-modal stability analysis are identical to those used in our previous modal stability analysis [19]. A simplified diagram of the computational domain, including its boundary conditions and coordinate system, is shown in Fig. 1(a) (not drawn to scale). The origin of the coordinate system is defined on the ground surface such that the leading edge of the airfoil is at $x = 0$. The x and y axes are defined parallel and perpendicular to the ground surface, respectively; see Fig. 1(a) for details. The computational domain is a rectangle with corners at $A(-10, 0)$, $B(-10, 15)$, $C(30, 15)$ and $D(30, 0)$. Therefore, $\overline{AB}$ defines the *inflow* boundary, $\overline{BC}$ and $\overline{CD}$ define the *outflow* boundary, and $\overline{AD}$ defines the *ground surface*. The airfoil is defined as a no-slip surface with a NACA 4415 profile. The ground clearance (h) is defined as the y-coordinate of the trailing edge of the airfoil, in the coordinate system described above. This value is non-dimensionalized by the chord length ($c = 1$). This implies that the x coordinate of the trailing edge is equal to $c\cos(\alpha)$, where α is in degrees.

The boundary conditions used in the computation of the base flow are the same as those used in our previous study [19]: (*inflow*) a Blasius boundary layer profile for velocity and a homogeneous Neumman boundary condition for pressure, (*outflow*) a homogeneous

Neumman boundary condition for velocity and a homogeneous Dirichlet boundary condition for pressure, and (*ground surface*) a no-slip and no-penetration boundary condition for velocity and a homogeneous Neumman boundary condition for pressure. The mesh contains around 2000 macro-elements (outlined by thick lines in Fig. 1b) and is refined using high-order Gauss-Lobatto-Legendre points. Domain-size independence of the energy gain $G(\tau)$ is demonstrated in Appendix A. In the present study, all the boundary conditions used in the stability analysis are of the Dirichlet homogeneous type:

$$\tilde{\mathbf{u}} = 0. \tag{8}$$

For most of this study, the angle of attack is kept at $\alpha = 20°$, although a few comparison tests involve the use of $\alpha = 12°, 15°$ and $18°$ as well. All four values of α are high enough to cause large-scale flow separation behind the airfoil, which is a unique feature of this study. The velocity and pressure fields are solved using `Nektar++` [24], an open-source code based on the spectral/hp element method [25, 26].

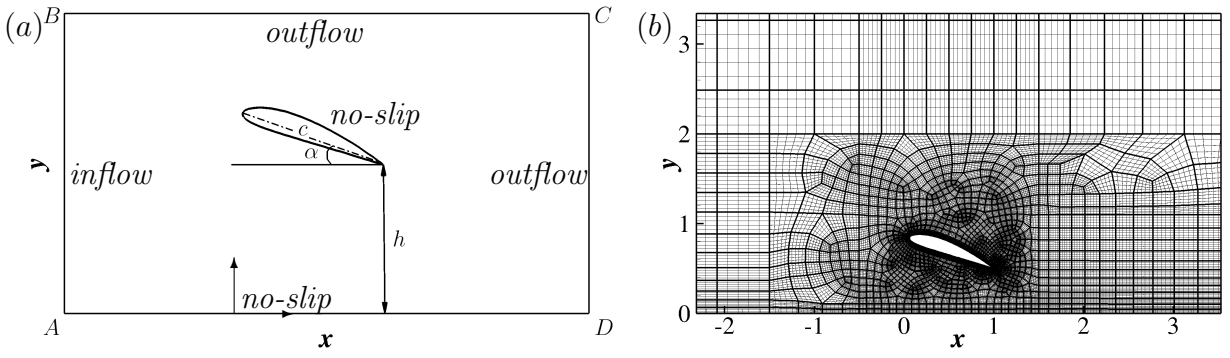

Fig. 1: (a) Diagram of the computational domain and its boundary conditions. The airfoil is not drawn to scale. (b) The mesh around the airfoil is refined using a polynomial of degree $p = 5$.

3. Results and discussion

3.1. Onset of global instability

The 2D base flows used in this study are taken from the DNS data of He et al. [19]. In the absence of a ground, the flow around a NACA 4415 airfoil at $\alpha = 20°$ is known to be unsteady when $Re \geqslant 300$, with the airfoil wake developing into a vortex street that oscillates self-excitedly in a limit cycle at a discrete natural frequency [19]. However, in the presence of a (no-slip) ground, the wake at $Re = 300$ becomes steady when $h \leqslant 0.5$, as shown in Fig. 2. Taking the case of $h = 0.3$ as an example (Fig. 2a), it can be seen that the flow wraps around the airfoil but then immediately separates from the leading and trailing edges, creating two recirculation zones that collectively make up a laminar separation bubble (LSB) behind the airfoil. The LSB is steady and its length in the streamwise direction (L_b), as measured from the trailing edge of the airfoil, is more than half a chord. When h increases to 0.5 (Fig. 2b),

the flow remains steady and qualitatively similar to that at $h = 0.3$ (Fig. 2a), although L_b increases to around a full chord length. A quantitative comparison of L_b can be found in Table 1.

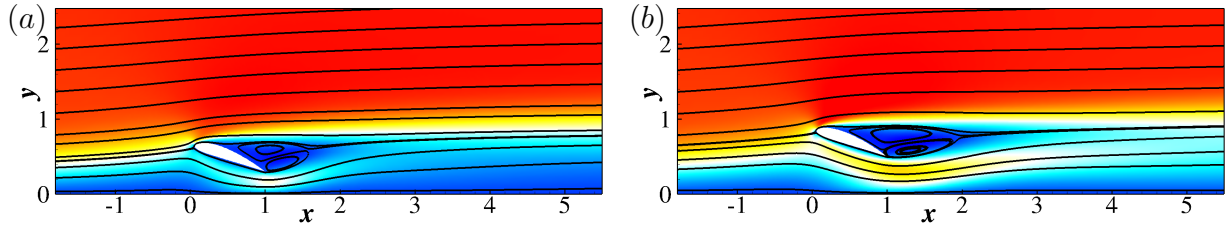

Fig. 2: Streamlines of the steady-state base flow around a NACA 4415 airfoil at $Re = 300$ and $\alpha = 20°$ for two different values of ground clearance: (a) $h = 0.3$ and (b) $h = 0.5$. For both values of h, the flow is naturally steady. The contour map shows the magnitude of the streamwise velocity.

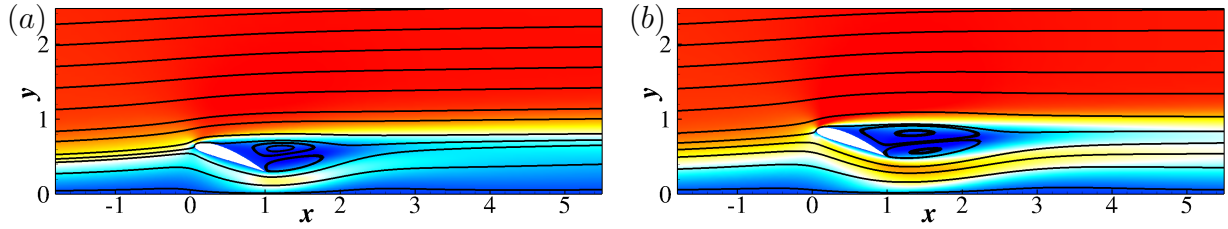

Fig. 3: The same as for Fig. 2 but at $Re = 500$: (a) $h = 0.3$ and (b) $h = 0.5$. The flow in (a) is naturally steady, but that in (b) is globally unstable, so selective frequency damping is used to extract a steady-state solution of the base flow. This base flow is then fed into the non-modal stability analysis of Sec. 3.2.

Table 1: Comparison of the magnitude of reverse flow ($u_{rev} \equiv u^-_{min}/u^+_{max}$) and the streamwise length of the LSB (L_b). Note that L_b is non-dimensionalized by the chord length of the airfoil.

Re	$h = 0.3$		$h = 0.5$	
	$u_{rev}(\%)$	L_b	$u_{rev}(\%)$	L_b
300	8.08	0.58	11.15	0.91
500	11.79	0.95	15.77	1.37

When Re increases to 500, the ground can still stabilize the wake, but only if $h \leqslant 0.35$ [19]. Figure 3(a) shows the streamlines of the steady flow field at $h = 0.3$ and $Re = 500$, whose features are remarkably similar to those at $h = 0.5$ and $Re = 300$ (Fig. 2b). When $h \geqslant 0.5$, however, the perturbations become amplified, causing the wake to transition from a globally stable state to a globally unstable state as the result of a sufficiently large region of local absolute instability [27]. The wake thus becomes unsteady, oscillating self-excitedly as a coherent vortex street with a discrete natural frequency (Fig. 4). In nonlinear dynamics,

this transition is referred to as a Hopf bifurcation, whereby the system switches from a fixed-point attractor to a limit-cycle attractor in phase space [28]. This type of transition is considered to be universal, appearing in a variety of self-excited flow systems, such as cylinder wakes [29], cross-flowing jets [30], jet diffusion flames [31, 32], low-density jets [33, 34, 35], turbulent ducted flames [36, 37], and turbulent reacting wakes [38]. When $h \geqslant 0.8$, the system becomes susceptible to secondary instabilities, which are dominated by short-wavelength (large β) 3D perturbations [19].

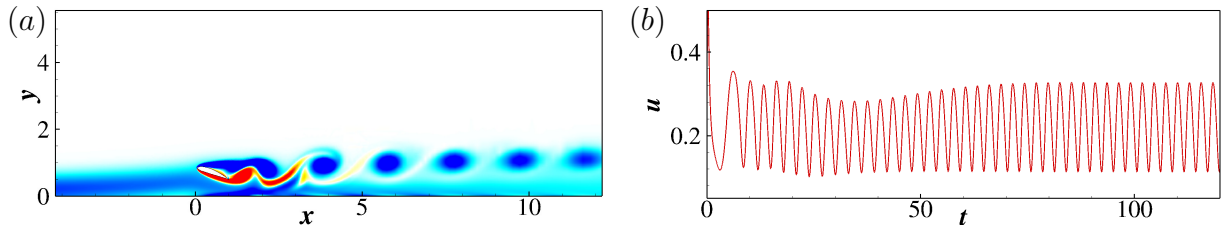

Fig. 4: (a) Vorticity contours showing vortex shedding behind a NACA 4415 airfoil at $Re = 500$ and $\alpha = 20°$ for a ground clearance of $h = 0.5$, and (b) time history of the streamwise velocity u during the first 120 time units at a location near the trailing edge of the airfoil.

To analyze the hydrodynamic stability of this unsteady flow, one needs a steady-state solution of the base flow, which we obtain via selective frequency damping [39]. This procedure involves filtering out the most unstable modes, leaving a steady but unstable solution of the Navier–Stokes equations, which is shown in Fig. 3(b) for $Re = 500$ and $h = 0.5$. Similar to the steady wake at $h = 0.3$ (Fig. 3a), the unsteady wake at $h = 0.5$ has a large LSB behind the airfoil. For $h = 0.5$, a higher shear stress arises in the recirculation zone and the boundary layer, resulting in a LSB about 25% longer than that for $h = 0.3$.

Figure 5 shows cross-stream profiles of the streamwise velocity $u(y)$ at three axial stations downstream of the airfoil ($x = 3$, 5 and 10), for two Reynolds numbers ($Re = 300$ and 500) and two ground clearances ($h = 0.3$ and 0.5). For $Re = 300$ (Fig. 5a), the velocity profile $u(y)$ has a pronounced inflection point in the boundary layer, downstream of the separation bubble, as can be seen at stations $x = 3$ and 5 for both $h = 0.3$ (solid lines) and $h = 0.5$ (dashed lines). According to Rayleigh's inflection-point theorem [40], this flow should be inviscidly unstable. The slope of the inflection point for $h = 0.5$ (dashed lines) is steeper than that for $h = 0.3$ (solid lines), which suggests that the instability is stronger for the former than it is for the latter. Farther downstream ($x = 10$), the $u(y)$ profiles for $h = 0.3$ and 0.5 begin to resemble each other, with a shallower slope at the inflection point, indicating a weakening of the underlying instability mechanism. This is consistent with the findings of Jones et al. [41], who showed that the local instability weakens with increasing x downstream of the separation bubble. Figure 5(b) shows the $u(y)$ profiles at the same three axial stations as Fig. 5(a), but for $Re = 500$ instead of $Re = 300$. As before, for both $h = 0.3$ (solid lines) and $h = 0.5$ (dashed lines), there is a clear inflection point in the boundary layer, which is particularly steep for $h = 0.5$, consistent with a globally unstable flow.

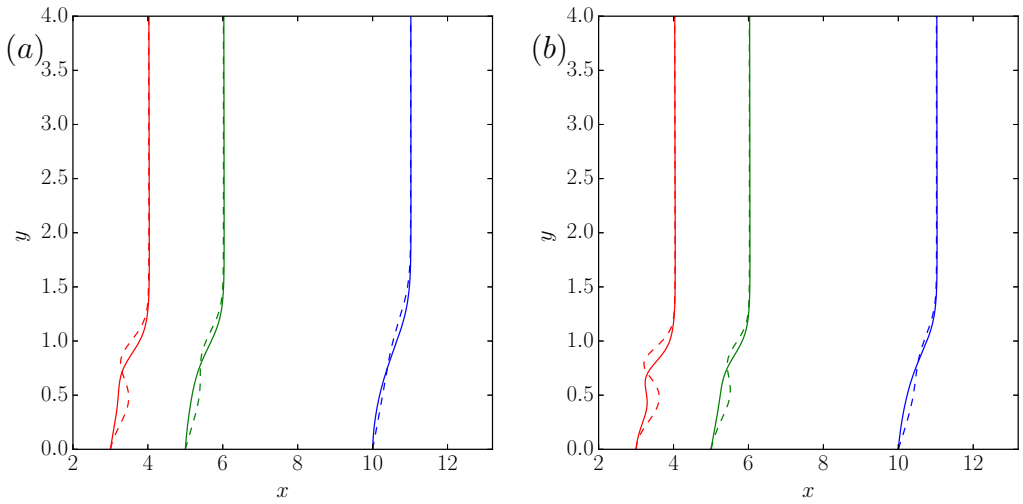

Fig. 5: Comparison of the streamwise velocity profile $u(y)$ in the boundary layer along a no-slip ground at three axial stations [$x = 3$ (red), 5 (green), 10 (blue)] downstream of the airfoil: (a) $Re = 300$ and (b) $Re = 500$. The solid and dashed lines represent data at $h = 0.3$ and 0.5, respectively.

For flow along a flat surface with a LSB, previous DNS and linear stability analyses have shown that a reverse flow velocity of more than 8% of the local free-stream velocity (i.e. $u_{rev} > 8\%$) is needed to produce convective instability and that $u_{rev} > 15\%$ is needed to produce absolute instability [42]. Analogous studies on hydrodynamic instabilities in flat-plate boundary layers with strong reverse flow have yielded similar conclusions [43, 44, 45]. The critical value of u_{rev} required to produce absolute/convective instability in the flow around a NACA airfoil without ground effect has been shown to be around 12–22% at low incidence ($\alpha = 5°$) and a high Reynolds number ($Re = 5 \times 10^4$) [41] and to be around 7% at high incidence ($10° \leqslant \alpha \leqslant 20°$) and low Reynolds numbers ($100 \leqslant Re \leqslant 300$) [18].

Table 1 compares the magnitude of reverse flow found in the LSB at the flow conditions of Fig. 2 ($Re = 300$) and Fig. 3 ($Re = 500$). Here, the magnitude of reverse flow is defined as $u_{rev} \equiv u^-_{min}/u^+_{max} \times 100\%$, where u^-_{min} and u^+_{max} are the minimum and maximum streamwise velocities, respectively. Note that u^-_{min} is in the $-x$ direction, whereas u^+_{max} is in the $+x$ direction. For the three naturally steady cases ($Re = 300$ with $h = 0.3$ and 0.5; $Re = 500$ with $h = 0.3$), u_{rev} remains below 12%, which is consistent with the view that these three flows are only locally convectively unstable (i.e. globally stable). By contrast, the flow at $Re = 500$ and $h = 0.5$ has a higher recirculation strength of $u_{rev} = 15.77\%$, which exceeds the critical threshold (15%) typically required for local absolute instability. A similar conclusion about the relationship between absolute/convective instabilities and the recirculation strength in the LSB was found by Alam and Sandham [42] using the mean flow defined in a turbulent boundary layer on a flat plate. Therefore, this could explain why this last flow oscillates periodically in a self-excited limit cycle [19]. This interpretation of the flow dynamics is supported by linear BiGlobal stability analysis showing that, at $Re = 500$, the growth rate of modal instabilities switches from negative to positive when h

increases from 0.3 to 0.5; see Fig. 6, which is adapted from Fig. 11 of Ref. [19]. Furthermore, this figure shows that, when $h \geqslant 0.8$, both the growth rate and frequency of the dominant modes remain relatively constant, indicating that the effect of the ground is strictly limited to conditions in which the airfoil is within 0.8 chord lengths from the ground surface. In view of this, we focus on investigating the non-modal stability for a ground clearance of $h = 0.3$ and 0.5 at different angles of attack ($12° \leqslant \alpha \leqslant 20°$).

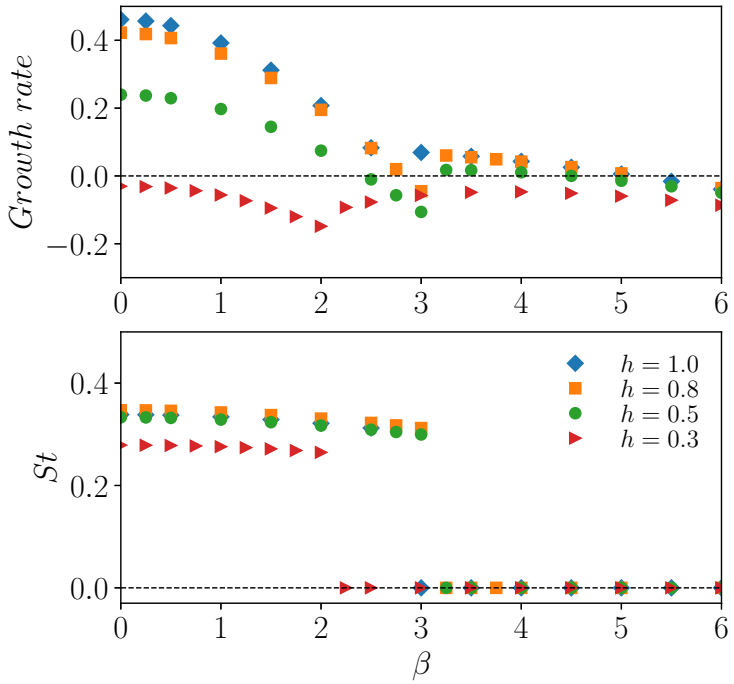

Fig. 6: (*top*) Growth rate and (*bottom*) Strouhal number of the leading eigenvalue, as calculated with linear BiGlobal stability analysis. The data are shown as a function of the spanwise wavenumber β for separated flow around a NACA 4415 airfoil at $Re = 500$, $\alpha = 20°$, and four different clearance heights above a flat no-slip ground surface ($0.3 \leqslant h \leqslant 1.0$). This figure is adapted from Ref. [19]. (Copyright 2018, Elsevier.)

3.2. Non-modal analysis: Transient growth

The growth of energy in a flow at short time horizons depends on the extent to which that flow is susceptible to non-modal instability. This can be quantified with the transient growth, as calculated in a non-modal stability analysis. Energy growth is caused by the non-normality of the eigenvectors [4]. The energy gain – as quantified by the energy amplification factor, $G(\tau)$ – in the wake of an airfoil without a ground at low Re and high α is known to be dominated by 2D optimal perturbations [18]. Revisiting this problem in the presence of a ground surface, we use a Krylov/Arnoldi method, implemented in *Nektar++*, to iteratively find the dominant eigenvalues and eigenvectors of $\mathcal{A}^{+}\mathcal{A}$ by time-step integration of the linearized direct and adjoint equations with a random initial perturbation for a given time horizon.

Figure 7 shows $G(\tau)$ as a function of the time horizon τ at $Re = 300$ for two values of ground clearance ($h = 0.3$ and 0.5) and three values of the spanwise wavenumber ($\beta = 0$, $\pi/4$ and $\pi/2$). For $h = 0.3$ (Fig. 7a), $G(\tau)$ is around $O(10^2$–$10^3)$ for all values of β, indicating relatively weak transient growth. Crucially, $G(\tau)$ for the 3D optimal perturbation ($\beta = \pi/4$) is higher than that for the 2D optimal perturbation ($\beta = 0$). This finding is contrary to the case without a ground, for which the 2D optimal perturbation shows the largest energy gain [16, 18]. This implies that, compared with the 2D optimal perturbation, the 3D optimal perturbation is more sensitive to the ground effect, becoming more readily amplified when the airfoil is close to the ground. However, when $h = 0.5$ (Fig. 7b), the 2D optimal perturbation ($\beta = 0$) dominates over the 3D optimal perturbation ($\beta = \pi/4$), with the energy gain $G(\tau)$ increasing to $O(10^3$–$10^4)$ at $\tau \approx 20$ before decaying with further increases in τ.

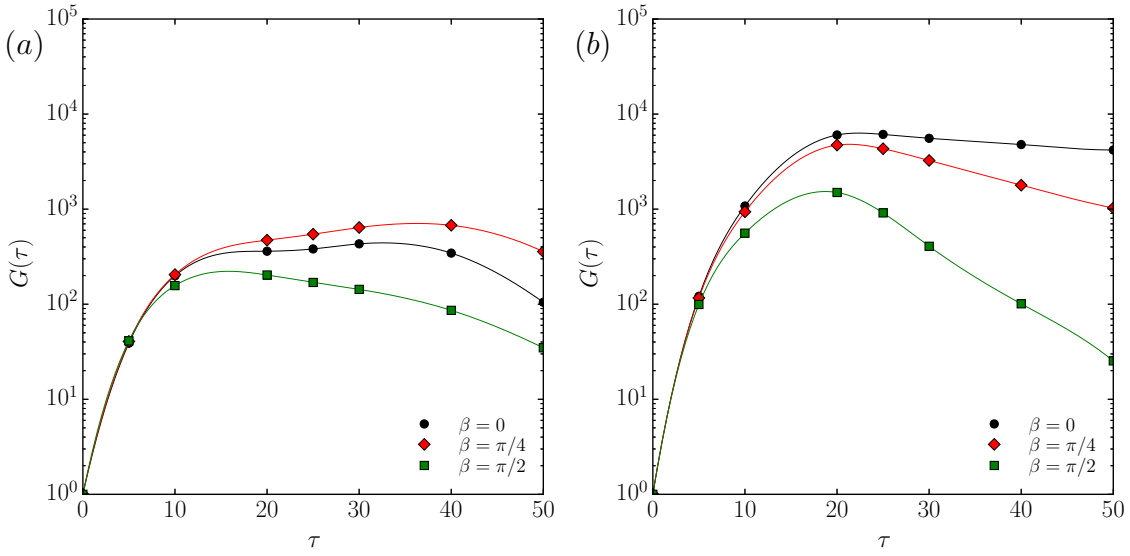

Fig. 7: Energy gain $G(\tau)$ as a function of the time horizon τ for separated flow around a NACA 4415 airfoil at $Re = 300$, $\alpha = 20°$, and two different values of ground clearance: (a) $h = 0.3$ and (b) $h = 0.5$.

When Re increases from 300 (Fig. 7) to 500 (Fig. 8), $G(\tau)$ also increases, indicating stronger transient growth. In Fig. 8, the spanwise wavelength varies from ∞ ($\beta = 0$; 2D case) to $2c$ ($\beta = \pi$). First we examine a case for which the ground clearance is small ($h = 0.3$). As Fig. 8(a) shows, $G(\tau)$ exceeds $O(10^4)$, which is nearly two orders of magnitude higher than that observed at the lower Reynolds number of $Re = 300$ (Fig. 7a). The initial growth rates of $G(\tau)$, as quantified by its slope with respect to τ, are reasonably similar across the different values of β, but the peak magnitude of $G(\tau)$ increases as $\beta \to 0$ (i.e. 2D perturbations), resulting in a difference of nearly two orders of magnitude between the maximum $G(\tau)$ at $\beta = 0$ and that at $\beta = \pi$. After peaking at around $\tau = 20$, $G(\tau)$ for the 2D optimal perturbation decays linearly with τ, which is consistent with the results of the modal stability analysis shown in Fig. 6. The 3D optimal perturbations show a similar decay with τ, although the trend is less linear. Both the 2D and 3D optimal perturbations

eventually evolve into the classical KH mode. According to modal stability analysis at $h = 0.3$ (Fig. 6), the growth rate of the 3D stationary eigenmodes at high β (e.g. $\beta = \pi$) is approximately equal to that of the 2D perturbations but do not oscillate in time.

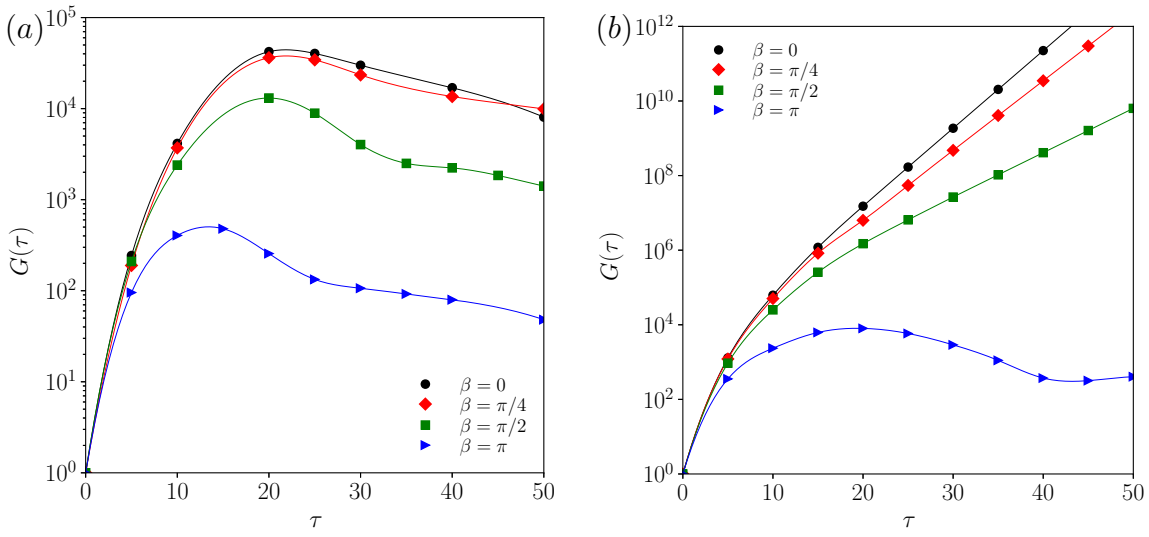

Fig. 8: The same as for Fig. 7 but at $Re = 500$: (a) $h = 0.3$ and (b) $h = 0.5$.

Next we consider flow at the same Reynolds number ($Re = 500$) but for a higher ground clearance (Fig. 8b: $h = 0.5$). For such a naturally periodic flow, Blackburn et al. [46] have computed the transient growth based on different phases in a period. For comparison, a time-independent steady-state flow obtained via selective frequency damping is considered here. We find that $G(\tau)$ increases linearly with τ in this log–linear plot, indicating exponential growth in a linear stability framework. In a real nonlinear flow system, however, the perturbations cannot grow indefinitely. The optimal perturbation produces no significant difference in the flow around a spanwise-homogeneous airfoil ($L_z > 8c$) when the ground clearance is small ($h = 0.3$), with the maximum $G(\tau)$ exceeding $O(10^4)$. In the flow around a small-aspect-ratio airfoil of two chord lengths ($\beta = \pi$), the optimal perturbation produces an energy gain of $O(10^2)$ at $\tau \approx 15$ before it decays. Although only partially shown, the slope of $G(\tau)$ at long time horizons converges asymptotically to the growth rate shown in Fig. 6. For instance, when $h = 0.3$, the growth rates are negative (Fig. 6), which implies convergence to a steady-state solution in Fig. 8(a). However, when $h = 0.5$, the growth rates are positive at small β (Fig. 6), which implies a divergent solution at long time horizons, typical of absolute instabilities, as shown in Fig. 8(b). This points to a strongly unstable flow dominated by 2D optimal perturbations, which is consistent with the results obtained from modal stability analysis (Fig. 6).

From Fig. 3, we recall that, when $h = 0.3 \to 0.5$, the flow undergoes a Hopf bifurcation, transitioning from a spatial amplifier of extrinsic perturbations (Fig. 3a: $h = 0.3$) to a self-excited oscillator with an intrinsic natural frequency (Fig. 3b: $h = 0.5$). The former state

is dominated by local convective instability, with no global oscillations, whereas the latter state is dominated by local absolute instability, with strong global oscillations prescribed by a wavemaker [27]. In Fig. 8(b), which is a log–linear plot, this transition to a global mode is found to coincide with a linear increase in $G(\tau)$, indicating exponential growth.

Figure 9 shows the normalized amplitude function of spanwise vorticity $\hat{\omega}_z$ at different times obtained by time integration of the LNSE, using the initial optimal perturbation as the initial condition, for two different values of ground clearance: (*left column*) $h = 0.3$ and (*right column*) $h = 0.5$. For the naturally steady flow ($h = 0.3$), the initial optimal perturbation is chosen at $\tau = 20$, which could trigger the maximum energy growth. This perturbation is defined in the boundary layer upstream of the airfoil, but is also strong at the leading edge of the airfoil, grows downstream with time, and then eventually decays – akin to a convectively unstable mode (see Fig. 8a). Finally, the perturbation is seen to evolve into classical KH modes, reminiscent of the results from previous studies [13, 18]. By contrast, for the naturally unsteady case ($h = 0.5$), the initial optimal perturbation defined at the same time horizon ($\tau = 20$) grows both spatially and temporally, giving rise to what appears to be an absolutely unstable mode (Fig. 8b). As in the previous case, this perturbation is particularly strong at the leading edge of the airfoil as well as throughout the separation bubble [Fig. 9(right column): outlined by a black line, indicating reverse flow], with an extended region of activity in the boundary layer upstream of the airfoil itself.

Figure 10 shows $G(\tau)$ as a function of τ for $Re = 500$, $h = 0.3$, $0 \leqslant \beta \leqslant \pi$, and four angles of attack: $\alpha = 12°$, $15°$, $18°$ and $20°$. In the lead up to $\tau = 5$, $G(\tau)$ grows similarly across all four values of α. Thereafter, however, $G(\tau)$ grows more strongly and for a longer time as α increases, reaching a local maximum whose τ and magnitude both increase with α. This demonstrates that the flow becomes less stable as α increases. It is worth noting that, across the time horizon $0 \leqslant \tau \leqslant 50$, $G(\tau)$ of the 2D optimal perturbation ($\beta = 0$) is consistently overtaken by that of the 3D optimal perturbation ($\beta = \pi/4$) when $\alpha = 12°$ and $15°$, but the former can sometimes exceed the latter when $\alpha = 18°$ and $20°$, indicating the existence of a crossover point delineating 2D and 3D dominance at $15° \leqslant \alpha \leqslant 18°$.

Figure 11 shows $G(\tau)$ under the same conditions as Fig. 10 but for a higher ground clearance ($h = 0.5$ vs $h = 0.3$). Here the flow becomes unstable when α increases from $12°$ to $15°$. At $\alpha = 12°$, a local maximum in $G(\tau)$ arises at around $\tau = 15$ for the 2D optimal perturbation ($\beta = 0$), with the small-wavenumber perturbations ($\beta = \pi/4$ and $\pi/2$) showing nearly the same amplitude. This could be due to a diminished separation zone behind the airfoil when $\alpha = 12°$. As α increases, the separation bubble grows spatially, causing the flow to become globally unstable. As Fig. 11(b–d) shows, the small-wavenumber optimal perturbations ($\beta = 0$, $\pi/4$ and $\pi/2$) are amplified such that their $G(\tau)$ increases linearly with τ in a log–linear plot, indicating exponential growth. As α increases, the degree (slope) of this growth also increases, and the 2D optimal perturbation ($\beta = 0$) begins to dominate the transient growth, whereas the large-wavenumber optimal perturbation ($\beta = \pi$) retains more or less the same $G(\tau)$. This shows that increasing α affects the small-wavenumber optimal perturbations ($\beta = 0$, $\pi/4$ and $\pi/2$) more than it affects the large-wavenumber optimal perturbations ($\beta = \pi$). In other words, the large-wavenumber optimal perturbations ($\beta = \pi$) are relatively insensitive to changes in α.

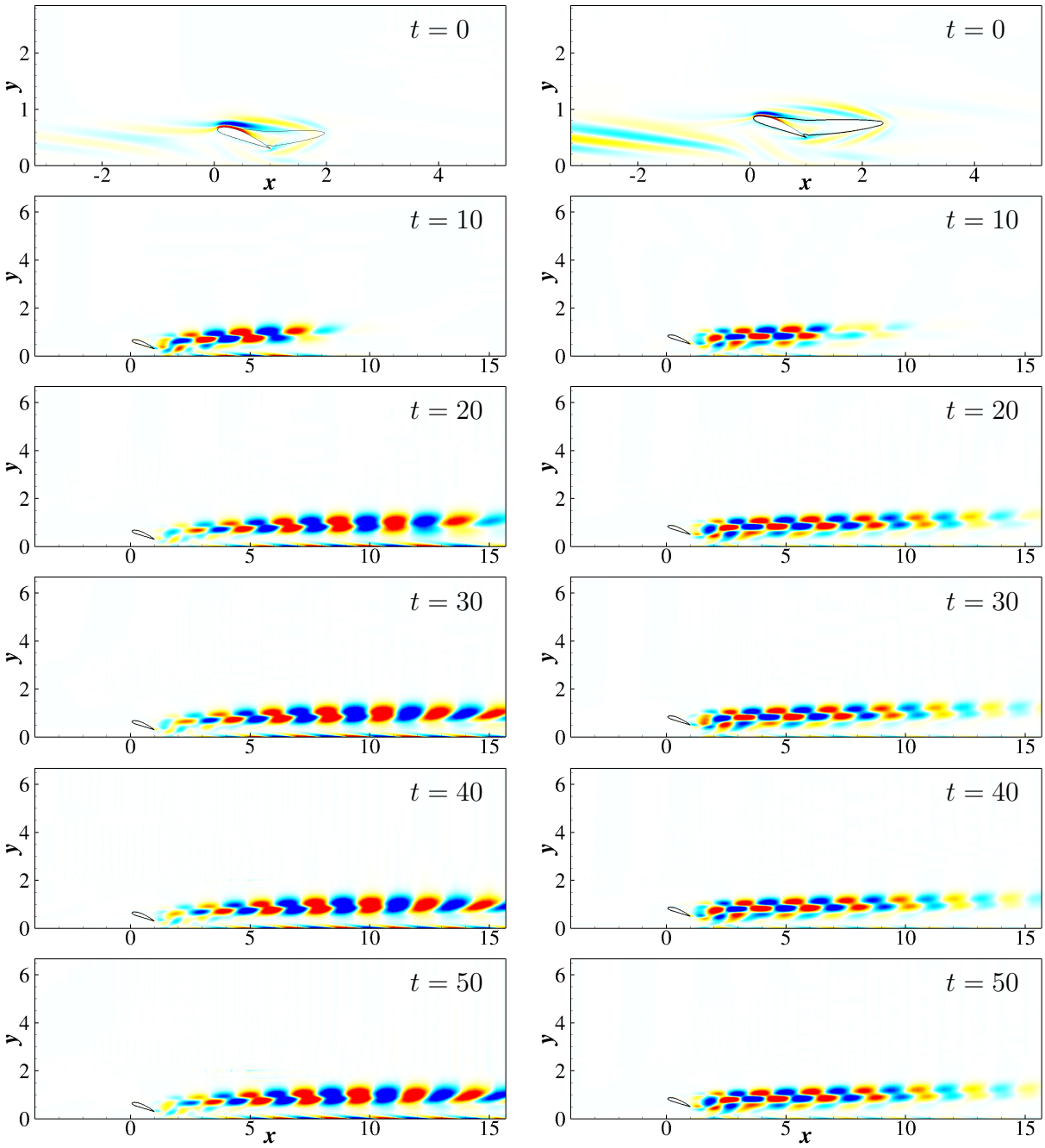

Fig. 9: Normalized amplitude function of spanwise vorticity $\hat{\omega}_z \in [-0.3, 0.3]$ at several different instants of the linear integration time t for the initial optimal perturbation at $\tau = 20$ (first row) at two different values of ground clearance: (*left column*) naturally steady flow at $h = 0.3$ and (*right column*) naturally unsteady flow at $h = 0.5$. The Reynolds number is $Re = 500$, and the angle of attack is $\alpha = 20°$.

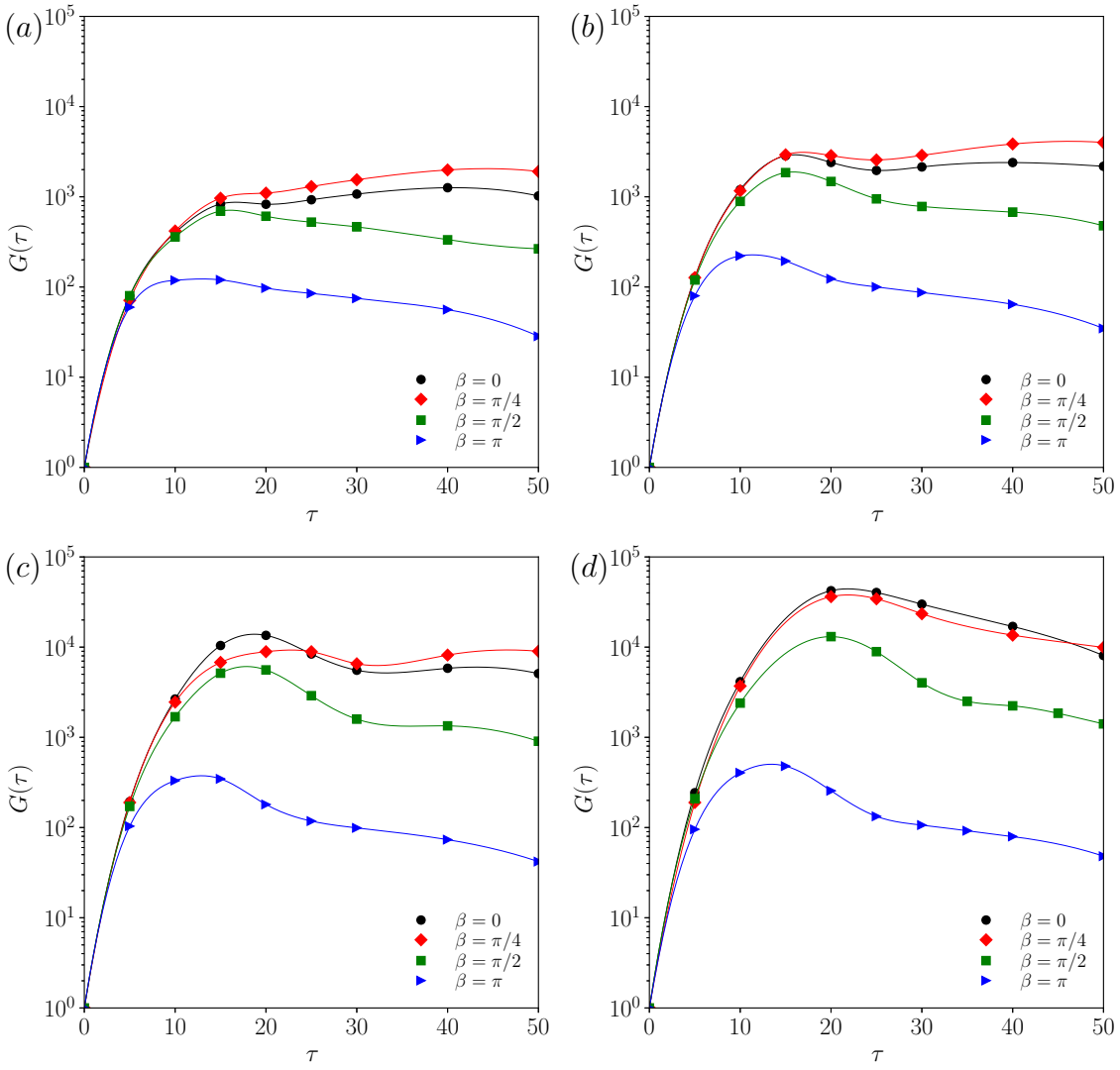

Fig. 10: Energy gain $G(\tau)$ as a function of the time horizon τ for separated flow around a NACA 4415 airfoil at $Re = 500$, $h = 0.3$, and four different values of the angle of attack: (a) 12°, (b) 15°, (c) 18°, and (d) 20°.

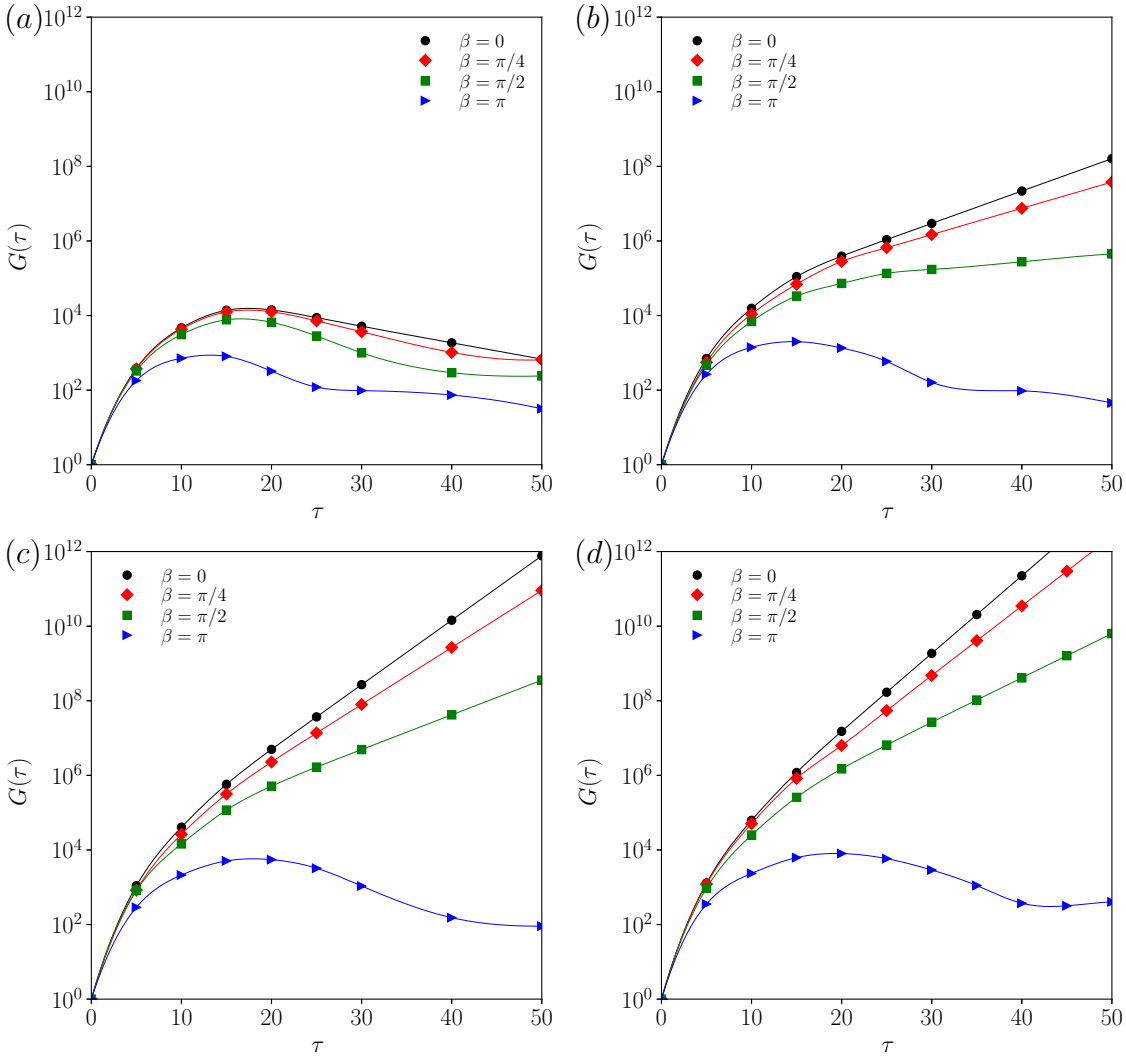

Fig. 11: The same as for Fig. 10 but at $h = 0.5$: (a) 12°, (b) 15°, (c) 18°, and (d) 20°.

3.3. Recovery of the Klebanoff mode in the boundary layer

For $Re = 500$ and $h = 0.3$ (Fig. 8a), the 3D optimal perturbation ($\beta = \pi/4$) produces the maximum energy gain at $\tau \approx 20$. The normalized final perturbation resulting from this is superimposed onto the homogeneous steady base flow at a disturbance level of $\epsilon = 0.0001$ in order to reconstruct the 3D total field using four oscillation periods, as shown in Fig. 12. The vorticity distribution of the total field is visualized with the λ_2 criterion. Downstream of the airfoil, the vortices are initially 'Ω' shaped, but are then increasingly pushed away from the ground as x increases. The vortices are mostly distributed along or across the edge of the boundary layer (Fig. 9). Farther downstream, at $x \approx 17$, classical 'Λ' vortices, or hairpin vortices, emerge close to the ground. These vortices, sometimes referred to as Klebanoff modes [47, 48, 49], are frequently observed in bypass transition in flat-plate boundary layers.

The vortices continue to grow downstream, which may indicate that, despite modal stability analysis showing that all of the perturbations are stable, the energy governed by non-modal or transient growth mechanisms can still be fed into the laminar flow, facilitating transition far downstream, as has been noted by Henningson [50].

In a boundary layer, Tollmien-Schlichting waves can develop from weak disturbances and grow downstream. Once their amplitudes become sufficiently high, they can break down into complex flow structures as nonlinear and 3D effects become active, ultimately leading to turbulence [51]. To explore transition in our airfoil-ground flow system, we perform 3D DNS by introducing an optimal initial perturbation of $\beta = \pi/4$ at $\tau = 20$ to a 2D steady flow at $Re = 500$ and $h = 0.3$. The perturbation is defined to be on the order of 1% of the base flow. Figure 13 shows the 3D instantaneous vortical structures at two time instants during the earlier stages of transition induced by high-amplitude optimal perturbations. In the regions immediately upstream and downstream of the airfoil, the flow is parallel and laminar. In the downstream wake (Fig. 13a), staggered and aligned Λ vortices can be seen coexisting in the boundary layer (for details, see Ref. [51]). As the flow evolves in time (from $t = 35$ to 40), the aligned mode begins to dominate the transition process (Fig. 13b). The main differences between the linear stability analysis and DNS are confined to a region around $10c$ downstream of the airfoil, although both methods can resolve the Klebanoff modes well. This may be attributed to the use of high-amplitude perturbations in the DNS. These results show that non-modal stability analysis can adequately predict the linear stages of transition in the airfoil-ground flow system studied here.

When h increases for $Re = 500$, the recirculation bubble collapses, and the resultant vortex shedding generates a stronger adverse pressure gradient in the boundary layer. The mechanism for downstream boundary-layer transition is mainly governed by long-wavelength secondary instability modes [19]. Similar findings have been observed in recent studies [52]. In the presence of strong recirculation, this could induce separation of the wall boundary layer. There is acceleration in the boundary layer just below the airfoil, as a result of the high α (i.e. the vertical clearance under the airfoil decreases from the leading edge to the trailing edge) and mass conservation, leading to a strong favorable pressure gradient. The resultant flow acceleration could increase the local Reynolds number, causing instabilities to emerge near the wall. Examining the detailed interaction between the wall vorticity layer and vortex shedding is best left for a future study.

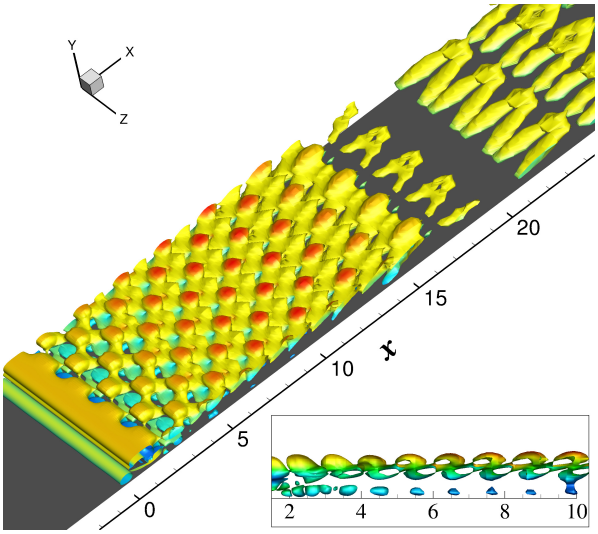

Fig. 12: 3D reconstruction of the total field at $Re = 500$ and $h = 0.3$. The total field, visualized via the Galilean invariant criterion $\lambda_2 = -0.01$ (colored by the streamwise velocity), is generated by superimposing the final optimal perturbation at $\tau = 20$ onto the steady-state base flow at a disturbance level of $\epsilon = 0.0001$. Hairpin vortices can be seen emerging downstream, close to the ground (gray). The inset shows a magnified side view of the cross-section of the vortices. The airfoil is partially obscured by the total field.

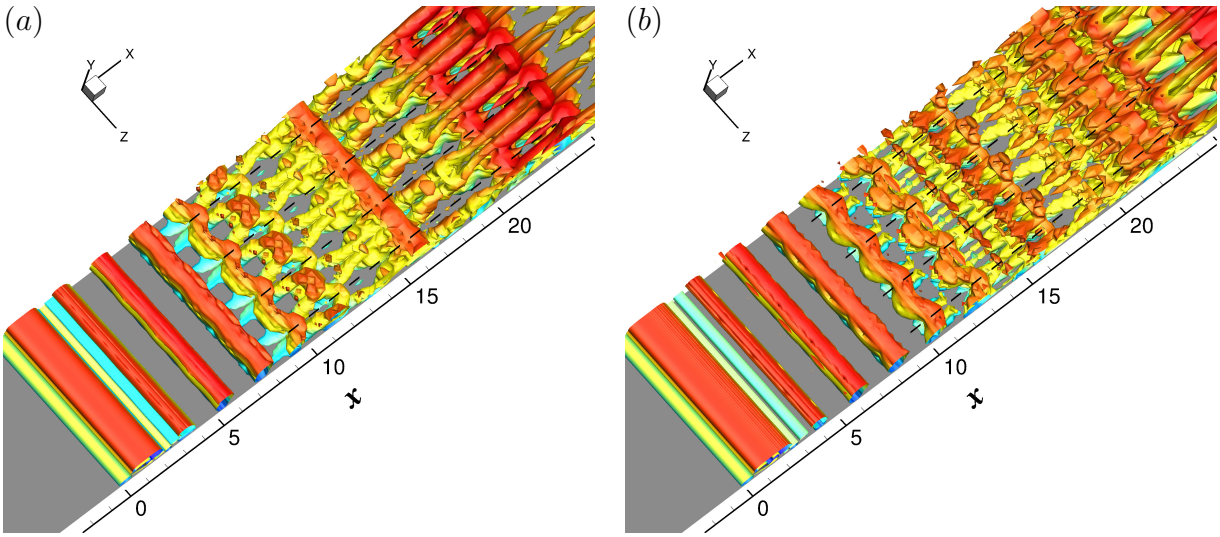

Fig. 13: Vortical iso-surface of $\lambda_2 = -0.01$ (colored by the streamwise velocity) computed via 3D DNS with an optimal initial perturbation of $\beta = \pi/4$ at $\tau = 20$ for (a) $t = 35$ and (b) $t = 40$. The four black dashed lines indicate the positions of the Λ vortices. The flow conditions ($Re = 500$ and $h = 0.3$) are the same as those in Fig. 12.

4. Conclusions

In this numerical–theoretical study, we have performed a linear non-modal stability analysis of the separated flow around a NACA 4415 airfoil over a no-slip ground at low Reynolds numbers ($300 \leqslant Re \leqslant 500$) and high angles of attack ($12^\circ \leqslant \alpha \leqslant 20^\circ$). By calculating the transient growth arising from 2D and 3D optimal perturbations, we find that the non-orthogonality of the eigenvectors can produce significant energy gain at short time horizons, even when the base flow is steady. For the flow conditions examined here, we find that: (i) the strength of the recirculation zone behind the airfoil is an important parameter governing the absolute/convective nature of the instability in the boundary layer downstream; (ii) when Re, α or h increases, $G(\tau)$ also increases, with the optimal perturbations switching from being 3D to 2D; and (iii) classical hairpin vortices, i.e. Λ vortices or Klebanoff modes, can be generated by 3D optimal perturbations on a 2D steady spanwise-homogeneous base flow containing a LSB. Knowledge of the spatiotemporal characteristics of the optimal mode can lead to improved strategies for flow control. This study provides new insight into the transient growth behavior of separated flow around a realistic airfoil in ground effect at low Re and high α. This insight could lead to an improved understanding of the ground-effect aerodynamics of micro aerial vehicles and small natural flyers.

Acknowledgments

We would like to thank the Research Grants Council of Hong Kong (Project Nos. 16235716 and 26202815) for their financial support. We would also like to thank Universidad Politécnica de Madrid and Southern University of Science and Technology for providing access to their computational resources.

Appendix A. Testing for domain-size independence

The sensitivity of the energy gain $G(\tau)$ to the size of the computational domain is investigated using five different domain sizes, as listed in Table A.2. Here a representative steady flow condition ($Re = 500$ and $h = 0.3$) is considered. M_1 is the smallest domain, with the shortest inflow length. M_2 and M_3 have the same cross-stream height as M_1, but both extend farther upstream and downstream, resulting in longer inflow and outflow lengths. M_4 and M_5 have the same inflow and outflow lengths as M_2 and M_3, respectively, but both extend farther in the cross-stream direction. From Table A.2, we can see that, for the domain sizes considered here, even the shortest outflow length is sufficiently long for it to have only a negligible influence on $G(\tau)$. However, both the inflow length and the cross-stream height have a marked influence on $G(\tau)$. Convergence is reached between M_4 and M_5; therefore, we use the full computational domain (M_5) to resolve the spatial evolution of the optimal perturbations. It is worth mentioning that we have cross-validated these results with an independent code, `Semtex` [53]. The resolution of the grid is identical to that used in our previous modal stability analysis [19].

Table A.2: Sensitivity of the energy gain $G(\tau)$ to the size of the computational domain at $Re = 500$, $h = 0.3$ and $\tau = 20$.

Mesh	x	y	$G(\tau)$
M_1	$[-6, 15]$	$[0, 7]$	4.19×10^4
M_2	$[-10, 15]$	$[0, 7]$	2.84×10^4
M_3	$[-10, 25]$	$[0, 7]$	2.86×10^4
M_4	$[-10, 15]$	$[0, 15]$	4.20×10^4
M_5	$[-10, 25]$	$[0, 15]$	4.22×10^4

References

[1] T. R. Bewley, S. Liu, Optimal and robust control and estimation of linear paths to transition, J. Fluid Mech. 365 (1998) 305–349.

[2] E. Åkervik, J. Hœpffner, U. Ehrenstein, D. S. Henningson, Optimal growth, model reduction and control in a separated boundary-layer flow using global eigenmodes, J. Fluid Mech. 579 (2007) 305–314.

[3] D. S. Henningson, A. Lundbladah, A. V. Johanson, A mechanism for bypass transition from localized disturbances in wall-bounded shear flows, J. Fluid Mech. 250 (1993) 169–207.

[4] S. C. Reddy, D. S. Henningson, Energy growth in viscous channel flows, J. Fluid Mech. 252 (1993) 209–238.

[5] L. N. Trefethen, A. E. Trefethen, S. C. Reddy, T. A. Driscoll, Hydrodynamic stability without eigenvalues, Science 261 (1993) 578–584.

[6] P. J. Schmid, Nonmodal stability theory, Annu. Rev. Fluid Mech. 39 (2007) 129–162.

[7] P. J. Schmid, D. S. Henningson, Stability and Transition in Shear Flows, Springer–Verlag New York, 2001.

[8] P. Luchini, Reynolds-number-independent instability of the boundary layer over a flat surface: optimal perturbations, J. Fluid Mech. 404 (2000) 289–309.

[9] S. Cherubini, J.-Ch. Robinet, P. D. Palma, The effects of non-normality and nonlinearity of the Navier–Stokes operator on the dynamics of a large laminar separation bubble, Phys. Fluids 22 (1) (2010) 014102.

[10] O. Marquet, D. Sipp, J.-M. Chomaz, L. Jacquin, Amplifier and resonator dynamics of a low-Reynolds-number recirculation bubbles in a global framework, J. Fluid Mech. 605 (2008) 429–443.

[11] H. M. Blackburn, D. Barkley, S. J. Sherwin, Convective instability and transient growth in flow over a backward-facing step, J. Fluid Mech. 603 (2008) 271–304.

[12] N. Abdessemed, A. S. Sharma, S. J. Sherwin, V. Theofilis, Transient growth analysis of the flow past a circular cylinder, Phy. Fluid 21 (2009) 044103.

[13] N. Abdessemed, S. J. Sherwin, V. Theofilis, Linear instability analysis of low pressure turbine flows, J. Fluid Mech. 628 (2009) 57–83.

[14] A. S. Sharma, N. Abdessemed, S. J. Sherwin, V. Theofilis, Transient growth mechanisms of low Reynolds number flow over a low-pressure turbine blade, Theor. Comp. Fluid Dyn. 25 (2011) 19–30.

[15] G. Rocco, T. A. Zaki, X. Mao, H. M. Blackburn, S. J. Sherwin, Floquet and transient growth stability analysis of a flow through a compressor passage, Aerosp. Sci. Technol. 44 (2015) 116–124.

[16] S. A. Loh, H. M. Blackburn, S. J. Sherwin, Transient growth in an airfoil separation bubble, in: 19th Australasian Fluid Mechanics Conference, Melbourne, Australia, Dec 8–11, 2014.

[17] R. S. Gioria, W. He, V. Theofilis, On global linear instability mechanisms of flow around airfoils at low Reynolds number and high angle of attack, Procedia IUTAM 14 (2015) 88–95.

[18] W. He, R. S. Gioria, J. M. Pérez, V. Theofilis, Linear instability of low Reynolds number massively separated flow around three NACA airfoils, J. Fluid Mech. 811 (2017) 701–741.

[19] W. He, P. Yu, L. K. B. Li, Ground effects on the stability of separated flow around a NACA 4415 airfoil at low Reynolds numbers, Aerosp. Sci. Technol. 72 (2018) 63–76.

[20] W. He, Y. Guan, V. Theofilis, L. K. B. Li, Stability of Low-Reynolds-Number Separated Flow Around an Airfoil Near a Wavy Ground, AIAA J. 57 (1) (2019) 29–34.
[21] V. Theofilis, Advances in global linear instability of nonparallel and three-dimensional flows, Prog. Aerosp. Sci. 39 (4) (2003) 249–315.
[22] V. Theofilis, Global linear instability, Annu. Rev. Fluid Mech. 43 (2011) 319–352.
[23] D. Barkley, H. M. Blackburn, S. J. Sherwin, Direct optimal growth analysis for timesteppers, Int. J. Numer. Meth. Fluids 57 (2008) 1435–1458.
[24] C. D. Cantwell, D. Moxey, A. Comerford, A. Bolis, G. Rocco, G. Mengaldo, D. D. Grazia, S. Yakovlev, J. E. Lombard, D. Ekelschot, B. Jordi, H. Xu, Y. Mohamied, C. Eskilsson, B. Nelson, P. Vos, C. Biotto, R. M. Kirby, S. J. Sherwin, Nektar++: An open-source spectral/hp element framework, Comput. Phys. Commun. 192 (2015) 205–219.
[25] A. T. Patera, A spectral element method for fluid dynamics: Laminar flow in a channel expansion, J. Comput. Phys. 54 (3) (1984) 468–488.
[26] G. Karniadakis, S. J. Sherwin, Spectral/hp element methods for computational fluid dynamics, Oxford University Press, 2nd edn., 2005.
[27] P. Huerre, P. A. Monkewitz, Local and global instabilities in spatially developing flows, Annu. Rev. Fluid Mech. 22 (1990) 473–537.
[28] R. C. Hilborn, Chaos and Nonlinear Dynamics, Oxford University Press, 2nd edn., 2000.
[29] M. Provansal, C. Mathis, L. Boyer, Bénard-von Kármán instability: Transient and forced regimes, J. Fluid Mech. 182 (1987) 1–22.
[30] J. Davitian, D. S. Getsinger, C. Hendrickson, A. R. Karagozian, Transition to global instability in transverse-jet shear layers, J. Fluid Mech. 661 (2010) 294–315.
[31] M. P. Juniper, L. K. B. Li, J. W. Nichols, Forcing of self-excited round jet diffusion flames, Proceedings of the Combustion Institute 32 (1) (2009) 1191–1198.
[32] L. K. B. Li, M. P. Juniper, Lock-in and quasiperiodicity in hydrodynamically self-excited flames: Experiments and modelling, P. Combust. Inst. 34 (1) (2013) 947–954.
[33] L. K. B. Li, M. P. Juniper, Lock-in and quasiperiodicity in a forced hydrodynamically self-excited jet, J. Fluid Mech. 726 (2013) 624–655.
[34] L. K. B. Li, M. P. Juniper, Phase trapping and slipping in a forced hydrodynamically self-excited jet, J. Fluid Mech. 735 (R5) (2013) 1–11.
[35] Y. Zhu, V. Gupta, L. K. B. Li, Onset of global instability in low-density jets, Journal of Fluid Mechanics 828.
[36] S. Balusamy, L. K. B. Li, Z. Han, M. P. Juniper, S. Hochgreb, Nonlinear dynamics of a self-excited thermoacoustic system subjected to acoustic forcing, Proceedings of the Combustion Institute 35 (3) (2015) 3229–3236.
[37] C. Y. Lee, L. K. B. Li, M. P. Juniper, R. S. Cant, Nonlinear hydrodynamic and thermoacoustic oscillations of a bluff-body stabilised turbulent premixed flame, Combust. Theor. Model. 20 (1) (2016) 131–153.
[38] B. Emerson, J. O'Connor, M. Juniper, T. Lieuwen, Density ratio effects on reacting bluff-body flow field characteristics, J. Fluid Mech. 706 (2012) 219–250.
[39] E. Åkervik, L. Brandt, D. S. Henningson, J. Hœpffner, O. Marxen, P. Schlatter, Steady solutions of the Navier–Stokes equations by selective frequency damping, Phys. Fluids 18 (2006) 068102.
[40] P. G. Drazin, W. H. Reid, Hydrodynamic Stability, Cambridge University Press, 2nd edn., 2004.
[41] L. E. Jones, R. D. Sandberg, N. D. Sandham, Direct numerical simulations of forced and unforced separation bubbles on an airfoil at incidence, J. Fluid Mech. 602 (2008) 175–207.
[42] M. Alam, N. D. Sandham, Direct numerical simulation of 'short' laminar separation bubbles with turbulent reattachment, J. Fluid Mech. 410 (2000) 1–28.
[43] U. Rist, U. Maucher, Investigations of time-growing instabilities in laminar separation bubbles, Eur. J. Mech. B/Fluids 21 (2002) 495–509.
[44] M. Embacher, H. F. Fasel, Direct numerical simulations of laminar separation bubbles: investigation of absolute instability and active flow control of transition to turbulence, J. Fluid Mech. 747 (2014)

141–185.
[45] D. Rodríguez, V. Theofilis, Structural changes of laminar separation bubbles induced by global linear instability, J. Fluid Mech. 655 (2010) 280–305.
[46] H. M. Blackburn, S. J. Sherwin, D. Barkley, Convective instability and transient growth in steady and pulsatile stenotic flow, J. Fluid Mech. 607 (2008) 267–277.
[47] P. S. Klebanoff, K. D. Tidstrom, Evolution of amplified waves leading to transition in a boundary layer with zero pressure gradient, NASA TN D–195, 1959.
[48] P. S. Klebanoff, Effect of free stream turbulence on a laminar boundary layer, Bull. Am. Phys. Soc. 16 (1971) 203–216.
[49] J. M. Kendall, Studies on laminar boundary layer receptivity to freestream turbulence near a leading edge, in: Boundary Layer Stability and Transition to Turbulence, vol. 114, ASME FED, 23–30, 1991.
[50] D. S. Henningson, Comment on "Transition in shear flows. Nonliear normality versus non-normal linearity"[Phys. Fluids 7, 3060 (1995)], Phys. Fluids 8 (8) (1996) 2257–2258.
[51] T. Herbert, Secondary instability of boundary layers, Annu. Rev. Fluid Mech. 20 (1988) 487–526.
[52] S. Hosseinverdi, H. F. Fasel, Role of Klebanoff modes in active flow control of separation: direct numerical simulations, J. Fluid Mech. 850 (2018) 954–983.
[53] H. M. Blackburn, S. J. Sherwin, Formulation of a Galerkin spectral element–Fourier method for three–dimensional incompressible flows in cylindrical geometries, J. Comput. Phys. 197 (2) (2004) 759–778.